Mathematical and Computational Modelling of MHD Effects in Entrained Droplets of Slag and Metal

Q.G. Reynolds[1]

[1] Mintek, Private Bag X3015, Randburg, 2125, South Africa; quinnr@mintek.co.za

ABSTRACT

A common mode of operation for electric smelting furnaces involves the availability of an open arc above the molten bath of process material. The plasma arc consists of a high-velocity, high-temperature jet of ionized gas, which imparts considerable mechanical stirring to the area in which it interacts with the surface of the bath. This stirring can result in significant inter-mixing and entrainment of the liquid phases in the bath, particularly in the vicinity of the arc attachment zone. Substantial electric current is also passed through this zone, either down through the slag and metal into the anode in the case of DC, or through the bath volume to the other electrodes in the case of AC.

The present study aims at quantifying the magneto-hydrodynamic (MHD) forces that result from the passage of electric current through and around droplets of one phase entrained in another. These forces can result in both intra-particle and inter-particle fluid dynamics, and generally act in opposition to surface tension and other forces. The OpenFOAM open-source framework is used to develop computational solvers based on the mathematical formulation of the problem. These tools are then applied to study the effect of current densities, diameters, interfacial surface tensions and other parameters on the droplet dynamics.

1 INTRODUCTION

Electric furnaces are widely used in the pyrometallurgy as melting and smelting unit operations. Applications include the production of primary and recycled steel, ferro-alloy production, ilmenite smelting, platinum-group metal concentration, and others [1]. The furnace technologies are used vary widely encompassing AC or DC current, single or multiple electrodes, and open-arc open-bath or submerged-with-burden operations.

A problem common to smelting furnaces of all types is the separation of the immiscible phases, for example slag from metal, within the vessel prior to tapping. This is both a quality concern (limit contamination of the product material with the waste phase), and an economic requirement (limit losses of the valuable product to the waste material). Certain furnace designs, for example open-arc high-current varieties, are capable of producing extremely violent mixing and stirring in the vicinity of the electrodes [2][3]. This agitation of the molten bath can cause substantial intermixing of the phases, and results in the generation of entrained particles across a large range of sizes between microns and centimetres. It is of some value to the process designer to gain a fundamental understanding of the various forces that can act on particles of one phase entrained in the other in these areas of high stirring energy.

In all types of electric furnaces, electric current must pass through one or more of the molten phases contained in the vessel in order to complete the circuit to the furnace power supply. In the case of single-electrode DC furnaces, the current path is through the electrode, through the plasma arc, through the slag and metal layers, and out through the hearth anode connection. In the case of AC three- or six-electrode furnaces, the current passes predominantly through the slag layer between electrodes. This is shown schematically in Figure 1.

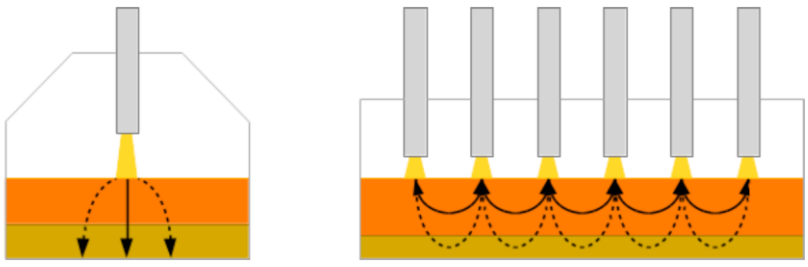

Figure 1: Current paths in DC (left) and AC (right) electric furnaces

The passage of current through the slag and metal baths in a smelting furnace generates magnetic fields, which in turn interact with the current paths to produce electromagnetic forces that act on the molten fluids. Together with surface tension and gravity, these are the primary forces that act on both the bulk fluid as well as particles of one phase

entrained in another. The electromagnetic forces scale in proportion to the square of the current density, and are therefore considerably larger in the areas near to the electrodes or arc attachment zones where the current flow is concentrated. Current densities of over 10^6 A/m^2 are possible in the slag zones immediately around plasma arcs [2].

The effect of electromagnetic forces on the bulk migration of entrained particles in slags, metals and mattes has been studied extensively [4][5]. This work has particular application to furnace technologies used for slag cleaning [6][7], and is highly relevant to the general phase separation problem in electric furnaces. The studies to date have focused largely on the behaviour of small spherical inclusions in the presence of independently generated magnetic and electric fields. Several effects were found to play a role in addition to simple gravitational settling, such as the electromagnetic buoyancy force (arising from a uniform background magnetic field) and electro-capillary motion (arising from the accumulation of electric charge near phase interfaces in ionic fluids such as slags).

Work on computational fluid dynamics modelling of the shape of droplets under the influence of gravitational and electromagnetic fields has also been published, although generally not in the area of smelting furnace technology. For example, Hyers et al. [8] examined the relative effects of forces acting on electromagnetically-levitated droplets and their effect on intra-droplet flow patterns. Amaya-Bower and Lee [9] performed detailed simulations of bubbles rising in liquids, and compared their results against a large body of previous computational modelling work.

A summary of the various forces that can act on a droplet of one phase suspended in another in the presence of a constant current density field **j** and a background magnetic field **B** is shown in Figure 2. The electro-capillary force acts in parallel with the current density vector, and the electromagnetic buoyancy force acts perpendicular to the plane of the current density vector and the magnetic field vector. In addition if the particle is more or less conductive than the surrounding phase, then the current density field becomes distorted around it – this sets up local variations in the magnetic field and results in additional "intra-particle electromagnetic" forces which act on the fluids inside and around the droplet.

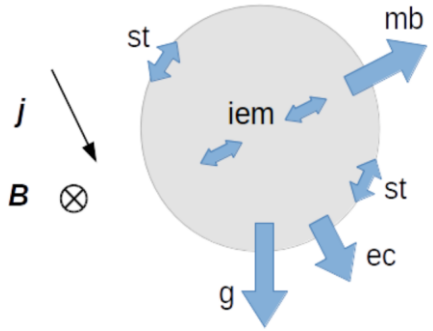

Figure 2: Forces acting on an entrained droplet (g: gravity, st: surface tension, ec: electro-capillary, mb: electromagnetic buoyancy, iem: intra-particle electromagnetic)

The interactions between the intra-particle electromagnetic forces, the surface tension forces, and gravity (as a proxy for all other external forces which act uniformly on the entire particle) and their impact on the shape and dynamics of the entrained particle will be the primary focus of this study. Inter-particle attraction and its effect on particle shape and coalescence will also be considered.

2 MATHEMATICAL MODELLING

Given certain assumptions, the electric and magnetic fields around entrained droplets have closed-form analytical solutions which are useful in assessing the order of magnitude of the forces involved. Let's consider an area of slag, through which a uniform current density $\mathbf{j_0}$ passes. If a highly conductive spherical metal droplet is inserted into this area, it distorts the current paths toward itself, and a larger current flows through the droplet compared to the surrounding slag. This is illustrated in Figure 3.

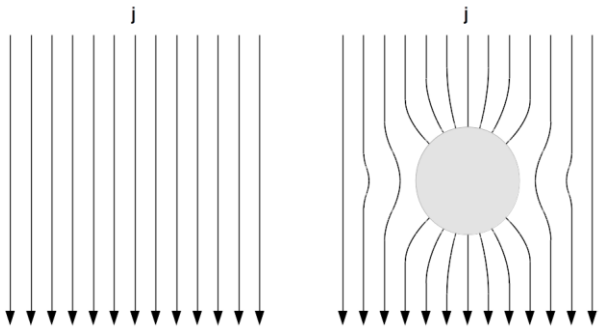

Figure 3: Current path distortion by infinitely conductive metal droplet entrained in slag

If the slag is assumed to have homogeneous and constant physical properties, and the metal droplet is assumed to be infinitely conductive, then the electric potential (voltage) field in the slag around the droplet is governed by the Laplace equation with appropriate boundary conditions. In spherical coordinates and assuming rotational symmetry, this is given by:

$$\frac{1}{r^2}\frac{\partial}{\partial r}\left(r^2\frac{\partial \Phi}{\partial r}\right)+\frac{1}{r^2\sin\theta}\frac{\partial}{\partial \theta}\left(\sin\theta\frac{\partial \Phi}{\partial \theta}\right)=0$$
$$\Phi\big|_{r=R}=0,\quad \left.\frac{\partial \Phi}{\partial r}\right|_{r=\infty}=E_\infty\cos\theta \tag{1}$$

Here, r and θ are the radial position and azimuthal angle respectively in a spherical coordinate system with origin located at the centre of the droplet, Φ is the scalar electric potential, E_∞ is the electric field strength in the surrounding slag far from the droplet, and R is the droplet radius. (1) may be solved by separation of variables to give the electric potential distribution in the slag around the droplet as a function of r and θ:

$$\Phi=E_\infty\left[1-\left(\frac{R}{r}\right)^3\right]r\cos\theta \tag{2}$$

From this, the current density field around the droplet can be determined:

$$\mathbf{j}=-\kappa_s\nabla\Phi=j_0\begin{pmatrix}-\left(1+2\left(R/r\right)^3\right)\cos\theta\\ \left(1-\left(R/r\right)^3\right)\sin\theta\\ 0\end{pmatrix}$$
$$\mathbf{j}=\mathbf{j}_{BG}+\mathbf{j}_{DF}=j_0\begin{pmatrix}-\cos\theta\\ \sin\theta\\ 0\end{pmatrix}+j_0\begin{pmatrix}-2\left(R/r\right)^3\cos\theta\\ -\left(R/r\right)^3\sin\theta\\ 0\end{pmatrix} \tag{3}$$

Here, κ_s is the electrical conductivity of the slag, and j_0 is the magnitude of the current density in the bulk phase far from the droplet ($j_0 = \kappa_s E_\infty$). From Maxwell's equations, this current density field in turn induces a self-magnetic field, given by:

$$\nabla \times \mathbf{B} = \mu_0 \mathbf{j}$$

$$\mathbf{B} = j_0 \mu_0 \begin{pmatrix} 0 \\ 0 \\ -\left(\frac{1}{2} + \left(R/r\right)^3\right) r \sin\theta \end{pmatrix} \tag{4}$$

$$\mathbf{B} = \mathbf{B}_{BG} + \mathbf{B}_{DF} = j_0 \mu_0 \begin{pmatrix} 0 \\ 0 \\ -\frac{1}{2} r \sin\theta \end{pmatrix} + j_0 \mu_0 \begin{pmatrix} 0 \\ 0 \\ -\left(R/r\right)^3 r \sin\theta \end{pmatrix}$$

Here, μ_0 is the magnetic permeability of free space. Due to the linearity of the governing equations, the current density and the magnetic field may both be separated into a background field BG and a distortion field DF as shown. The background fields are those that would exist in the absence of the entrained droplet, and the distortion fields represent the perturbation of the background fields by the presence of the droplet.

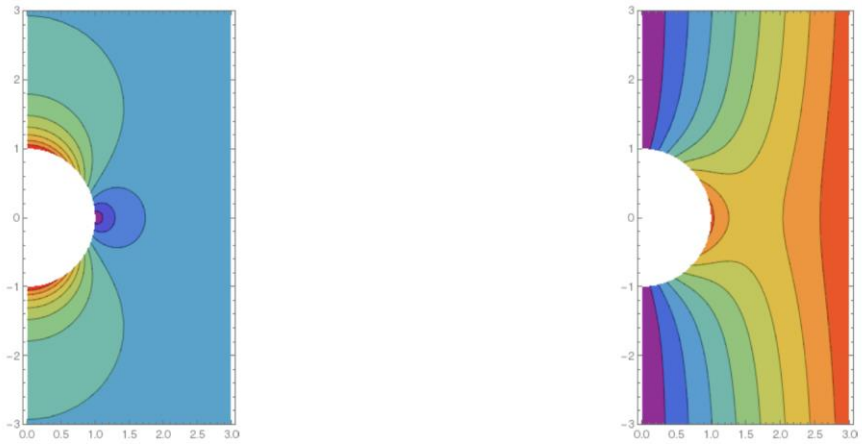

(a) $|\mathbf{j}|/j_0$ *(b)* $|\mathbf{B}|/j_0\mu_0$

Figure 4: Distribution of (a) current density field and (b) magnetic field around an infinitely conductive spherical droplet in vertical and radial (r/R) directions

An example of the magnitude of the current density and magnetic field vectors around a droplet of metal entrained in a slag phase is shown in Figure 4. Both images scale from close to zero (purple and blue) to three (red), indicating the current-concentrating effect of the droplet.

2.1 Comparison of forces acting on a single droplet

Once the electric and magnetic fields around an entrained droplet are known, the net force acting on the droplet as a result of the distortion of the fields by its presence can be calculated. This is done by integrating the r-component of the Lorentz force vector, **j** x **B**, over the volume of slag around the droplet and considering only the contributions from the distortion field components.

$$F_{iem} = \int_R^\infty \int_0^{\pi/2} 2\pi \left(\mathbf{j}_{DF} \times \mathbf{B}_{DF}\right)_r r^2 \sin\theta \, d\theta \, dr$$
$$= -\frac{2}{3} \pi \mu_0 j_0^2 R^4 \tag{5}$$

This shows that the electromagnetic forces acting on entrained metal particles are compressive, and scale very aggressively with the particle size (and to a lesser degree with the current density in the surrounding material).

It is interesting to compare this result with the surface tension forces acting on the boundary of the droplet. These act uniformly around the perimeter of the droplet to create a spherical shape, whereas the electromagnetic forces act unevenly to distort the droplet shape. The surface tension forces acting on a spherical droplet are given by [10]:

$$F_{st} = 2\pi R\gamma \tag{6}$$

Here, γ is the surface tension of the slag-metal interface. Finally, the gravitational force acting to accelerate the droplet through the surrounding phase is given by:

$$F_g = \tfrac{4}{3}\pi g \Delta\rho R^3 \tag{7}$$

Here, Δρ is the difference in densities between slag and metal, and g is gravitational acceleration. As it is the interplay between these three forces that produce changes in the droplet's shape and dynamic behaviour, it is of some interest to compare these under different conditions. This comparison is shown in Figure 5.

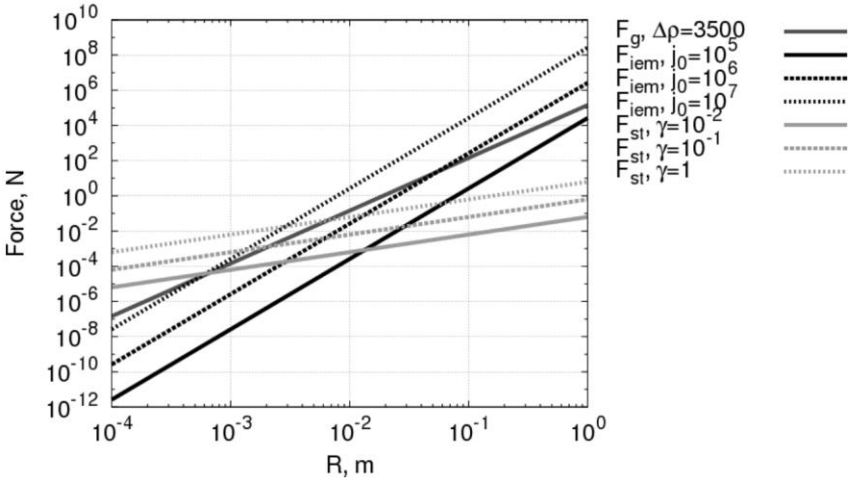

Figure 5: Comparison of (5), (6) and (7) for typical values of j_0 and γ (units: [ρ] = kg/m^3, [j_0] = A/m^2, [γ] = N/m)

At very small droplet radii typical of prills and finely-dispersed entrained particles, the surface tension force dominates the gravitational and electromagnetic forces and the particle is likely to remain spherical while settling. At large scales of a few centimeters typical of entrainment in the high-energy mixing zones near the arcs in electric furnaces, the electromagnetic forces dominate. In the region between approximately 1mm and 1cm droplet size, the forces are of comparable magnitude and the particle's final shape and dynamics (steady-state or transient) are likely to be highly variable.

2.2 Slag droplet entrained in metal

For the opposite case, that is, an infinitely *resistive* slag droplet entrained in a conductive metal phase, the analysis proceeds similarly with the exception of a different boundary condition at the surface of the droplet. Instead of Φ = 0, the boundary condition for (1) becomes:

$$\left.\frac{\partial\Phi}{\partial r}\right|_{r=R} = 0 \tag{8}$$

This gives a slightly different solution for the electric potential field around a slag droplet entrained in metal:

$$\Phi = E_\infty\left[1+\frac{1}{2}\left(\frac{R}{r}\right)^3\right]r\cos\theta \tag{9}$$

By inspection and comparison with (2), it can be seen that the magnitude of the distortion in the electric potential field produced by a slag droplet embedded in a metal phase is only half of that produced by a metal droplet entrained in slag. This factor carries through to the calculation of both the current density and the self-magnetic field, and the electromagnetic compression force is only one quarter as strong as it is in the case of metal droplets in slag.

Surface tension would therefore be expected to play a greater role in the evolution and dynamics of slag droplets entrained in metal.

2.3 Attractive force between droplets

If two (or more) entrained metal droplets are located close to one another in the slag phase, an attractive force will exist between them due to the increased current density within the droplets and their resulting magnetic fields; this is analogous to the attractive force between two parallel conductors carrying current in the same direction. The magni-

tude of this force may be approximated by assuming that the current density within the metal droplet is constant, and that the magnetic field of one droplet acting on another is constant for a given separation between the droplets. The average current density inside a droplet acting in the vertical direction is calculated by integrating the current density from (3) over one hemisphere of the droplet, and then dividing by the droplet's cross-sectional area. This gives:

$$j_{zDF} = -2 j_0 \tag{10}$$

Here, j_{zDF} is the deviation of the current density above the background field, indicating that the current density inside the droplet is three times higher than the current density in the surrounding slag.

If the droplets are positioned in the way the line between their centres is perpendicular to the direction of the current flow, then the magnetic field generated by one droplet and felt by another may be approximated as follows:

$$B_{\phi DF} = -\mu_0 j_0 R \left(\frac{R}{x_s} \right)^2 \tag{11}$$

Here, B_{DF} is the strength of the magnetic field generated by the first droplet that is felt at the centre of the second droplet (assumed to be constant over the volume of the second droplet), and x_s is the centre-to-centre separation distance between the two droplets. Integrating the Lorentz force, **j** x **B**, over the volume of the second droplet then gives the attractive force it experiences as a result of the first droplet:

$$F_{c-c} = \tfrac{4}{3} \pi \mu_0 j_0^2 R^4 \left(\frac{R}{x_s} \right)^2 \tag{12}$$

Here, F_{c-c} is the force that is experienced by each droplet according to Newton's second law. The relationship (12) is shown in Figure 6 with (5) included for comparison.

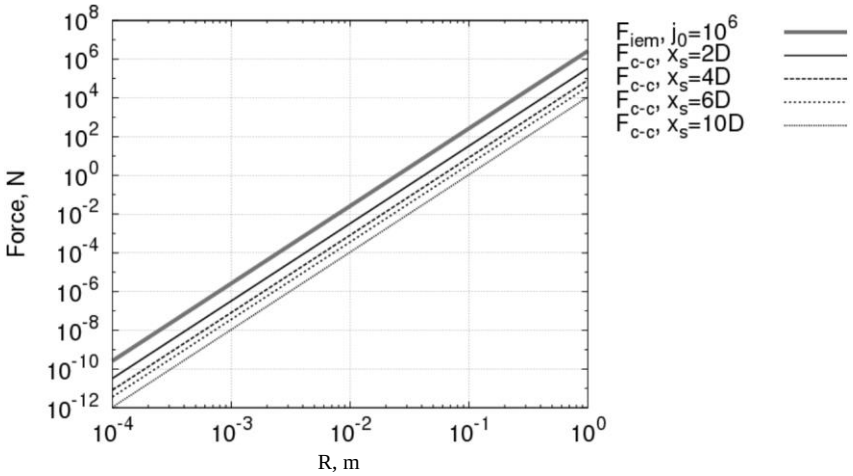

Figure 6: Graph showing dependence of inter-particle attraction force on particle size and separation (D = 2R)

Although it is only a rough approximation, it can be seen that for moderate droplet separation distances the intra-particle forces exceed the inter-particle force by an order of magnitude or more - the droplets must approach each other very closely indeed before the attractive force becomes significant. This suggests that attraction between entrained droplets is likely to be a second-order effect as compared to the interaction between surface tension and intra-particle electromagnetic forces, and highlights the importance of good stirring in getting droplets to coalesce.

3 COMPUTATIONAL MODELLING

In order to study the dynamics of entrained droplets in more detail, a "numerical experiment" approach using computational modelling methods was adopted. Droplets settling under the influence of gravity only were studied initially to provide model validation data, with electromagnetic effects included in the full droplet MHD model.

3.1 Dimensional considerations

In order to correctly parameterize the problem, dimensional analysis of a single entrained droplet developing under the influence of gravity, surface tension, and electromagnetic forces was conducted. The relevant variables in this case are the equivalent spherical diameter of the droplet (D), density (ρ) and viscosity (μ) of the droplet and the

surrounding phase, the interfacial surface tension (γ) between the droplet and the surrounding phase, acceleration due to gravity (g), the magnetic permeability of free space (μ_0), and the magnitude of the bulk current density passing through the material (j_0). Unless otherwise specified, subscript "s" refers to the surrounding phase, and subscript "m" refers to the droplet phase.

For this set of variables and fundamental units, five dimensionless groups are required to fully characterize the droplet behaviour. The dimensionless parameters shown in Table 1 were constructed using the standard Buckingham π method.

Here, N_{Eo} and N_{EM} are standard and electromagnetic forms of the Eötvös number, N_{Mo} is the Morton number, and N_V and N_d are the ratios of phase viscosity and density respectively. ρ_m is assumed to be greater than ρ_s in this case. It is interesting to observe that apart from some constants of proportionality N_{Eo} is obtained directly from the ratio of (7) and (6), and N_{EM} is obtained from the ratio of (5) and (6) – the Eötvös numbers therefore quantify the relative strength of the various forces acting on the droplet.

Table 1: Dimensionless parameters for droplet MHD problem

Parameter	*Formula*	*Parameter*	*Formula*
N_{Eo}	$\frac{g(\rho_m-\rho_s)D^2}{\gamma}$	N_V	$\frac{\mu_m}{\mu_s}$
N_{Mo}	$\frac{g\mu_s^4(\rho_m-\rho_s)}{\gamma^3\rho_m^2}$	N_d	$\frac{\rho_m}{\rho_s}$
N_{EM}	$\frac{\mu_0 j_0^2 D^3}{\gamma}$		

In the typical metal-slag systems of interest in this study the phase viscosities are usually very different ($N_v < 10^{-2}$), and the phase densities fall within a reasonably narrow range ($N_d \sim 2 \pm 0.5$). The effect of these two parameters will therefore not be considered here.

3.2 Computational model formulation

The Navier-Stokes and continuity equations with standard Newtonian shear stresses are used to describe the fluid flow across all phases:

$$\rho\frac{\partial \mathbf{v}}{\partial t}+\nabla\cdot(\rho\mathbf{v}\mathbf{v})+\nabla P=\nabla\cdot(\mu\nabla\mathbf{v})+\mathbf{j}\times\mathbf{B}+\rho\mathbf{g} \quad (13)$$

$$\frac{\partial \rho}{\partial t}+\nabla\cdot(\rho\mathbf{v})=0 \quad (14)$$

Here, **v** is the velocity vector field, and P is the pressure field. μ and ρ are the fluid viscosity and density fields calculated as a volume average of the phase field. As before **j** x **B** is the Lorentz force resulting from the current density and magnetic fields, and **g** is the gravitational acceleration vector.

In problems involving the flow of electricity, Maxwell's equations govern the electromagnetic fields generated and must be solved simultaneously with the fluid flow equations:

$$\begin{aligned}&\mathbf{j}=\kappa\left(-\nabla\Phi-\frac{\partial\mathbf{A}}{\partial t}+\mathbf{v}\times(\nabla\times\mathbf{A})\right)\\&\nabla\cdot\mathbf{j}=0\\&\nabla^2\mathbf{A}=-\mu_0\mathbf{j}\end{aligned} \quad (15)$$

Here, **A** is the magnetic vector potential (**B** = ∇ x **A**) using the Coulomb gauge, κ is the electrical conductivity field of the fluid, and Φ is the (scalar) electric potential field.

The droplet MHD problem was implemented using version 2.3.1 of the OpenFOAM open-source framework for field solution of conservation equations [11]. Extension of OpenFOAM's standard multiphase fluid flow solver, *interFoam*, to include numerical solution of Maxwell's equations was performed, resulting in two new solvers (*interFoamEM* and *interDyMFoamEM* for static and dynamic mesh problems respectively).

Within the solvers, the volume-of-fluid (VOF) algorithm was used to take account of the phase separation. This involves solution of a separate convective transport equation for the volume fraction field of each phase which

amounts to approximation of the two-phase system as a single phase flow problem with appropriate source terms at the phase interface. The Pressure Implicit with Splitting of

Operators (PISO) predictor-corrector algorithm was used for calculation of the velocity and pressure fields at each time step. Gradient-limited discretisations were used for all divergence terms with the exception of those related to the phase fraction fields used the specialised Multidimensional Universal Limiter for Explicit Solution (MULES) interface compression method. Adaptive time-stepping was used in order to maintain a Courant number of 0.5 or below for numerical stability. Solution of the electromagnetic fields was accomplished using an iterative algorithm solving each of the equations in (15) successively until convergence for the time-step was achieved.

Simple boundary conditions were supplied to represent free inflow and outflow of fluid as the droplet moves through the region, and a constant current density far from the droplet. A zero-velocity initial condition was used to permit observation of the evolution of the droplet shape and position from stagnant conditions.

Meshing of the model region was performed using Python scripts implementing OpenFOAM's blockMesh tool. High-resolution static meshes were used for the 2D modelling work, while dynamic adaptive meshing was applied in the 3D model calculations.

3.3 Model results – gravity settling

In order to validate the multiphase flow component of the computational model, electromagnetic effects were disregarded at first. This results in simple gravity settling of a droplet with surface tension, and has been well studied by other workers [10][12]. Axisymmetric, two-dimensional simulations of a single droplet of metal settling through a slag phase were conducted at several different values of N_{Eo} and N_{Mo} in order to compare the shape deformation and dynamic behaviour of the system with published results.

The parameters used for this set of cases are shown in Table 2.

Table 2: Model parameters for gravity settling

Parameter	*Value*	*Parameter*	*Value*
D	0.5 – 50 mm	γ	0.01 - 1 N/m
μ_s	0.1 Pa.s	ρ_s	3500 kg/m^3
μ_m	0.006 Pa.s	ρ_m	7000 kg/m^3
Mesh resolution	50000 elements	Mesh dimensions	2.5D x 10D

The evolution of the shape and position of an 8 mm metal droplet falling through surrounding slag is shown in Figure 7.

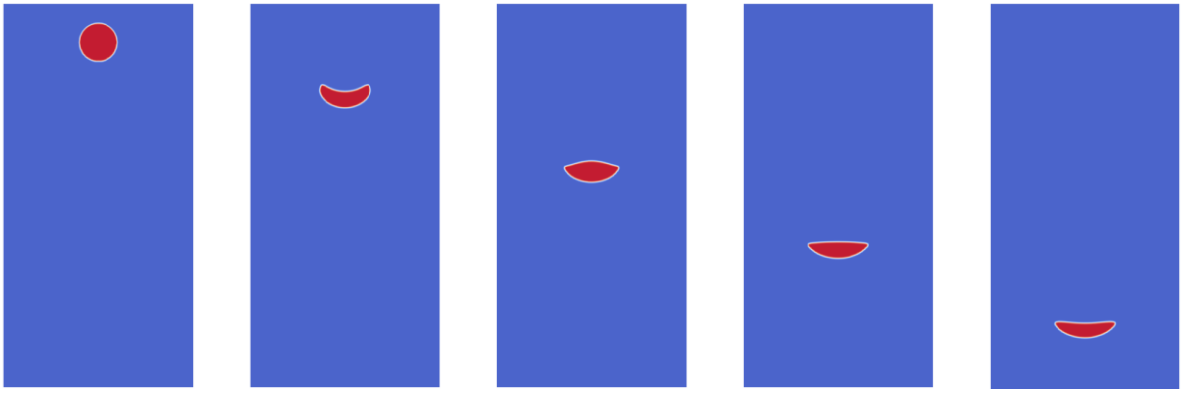

(a) 5 ms *(b) 100 ms* *(c) 200 ms* *(d) 300 ms* *(e) 400 ms*

Figure 7: Metal (red) droplet settling through slag (blue), D = 8 mm, γ = 0.1 N/m

The interaction between the two fluid phases in this case produces considerable deformation of the droplet as it settles. The shape and settling velocity in such situations was well characterized by Weber et al. [10] who presented the Reynolds number of the droplet at terminal velocity as well as qualitative descriptions of the droplet shapes over a wide range of N_{Eo} and N_{Mo}. A series of simulations using the computational model were run, and the results were compared against literature values.

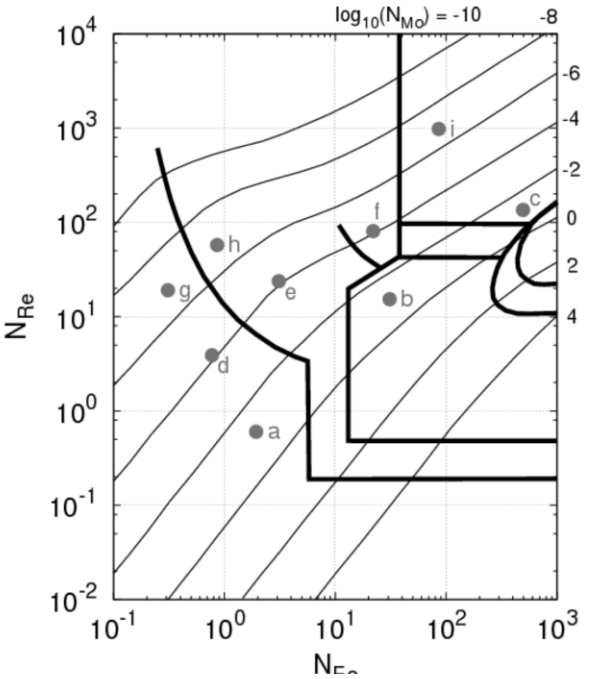

Figure 8: Graph showing position of simulation results in droplet shape zones

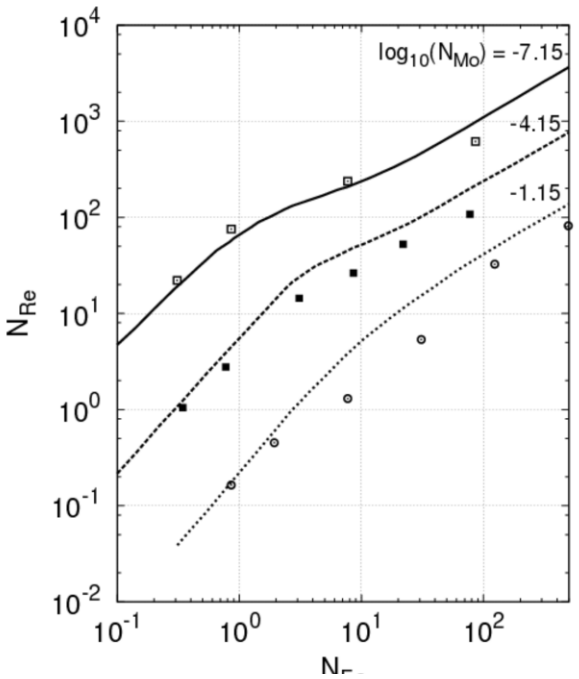

Figure 9: Graph showing comparison of terminal velocities from literature and modelling results

Figure 8 shows the location of several of the simulations performed using the computational model on a chart of droplet shape zones as a function of N_{Eo} and N_{Mo}. a, d, and g are located in the "spherical" zone, b in the "oblate ellipsoidal cap" zone, c and i in the "open, unsteady wake" zone, e and h in the "oblate ellipsoid" zone, and f in the "oblate ellipsoidal, disk-like and wobbling" zone [12]. Droplet shapes generated by the model for conditions a to i are shown in Figure 10, and are seen to be generally in good agreement with the shape zones from literature.

Terminal velocity u_t was estimated for each simulation by calculating the average velocity in the vertical direction at the end of the run, over all elements in the computational model that contained a majority of metal. This was then used together with the droplet's original spherical diameter D to calculate a representative Reynolds number, $N_{Re} = Du_t\Delta\rho/\mu_s$. The model data (points) are compared to correlation data (lines) from [12] in Figure 9, and the results are seen to agree quite well, particularly under the high surface tension conditions typical of slag-metal systems.

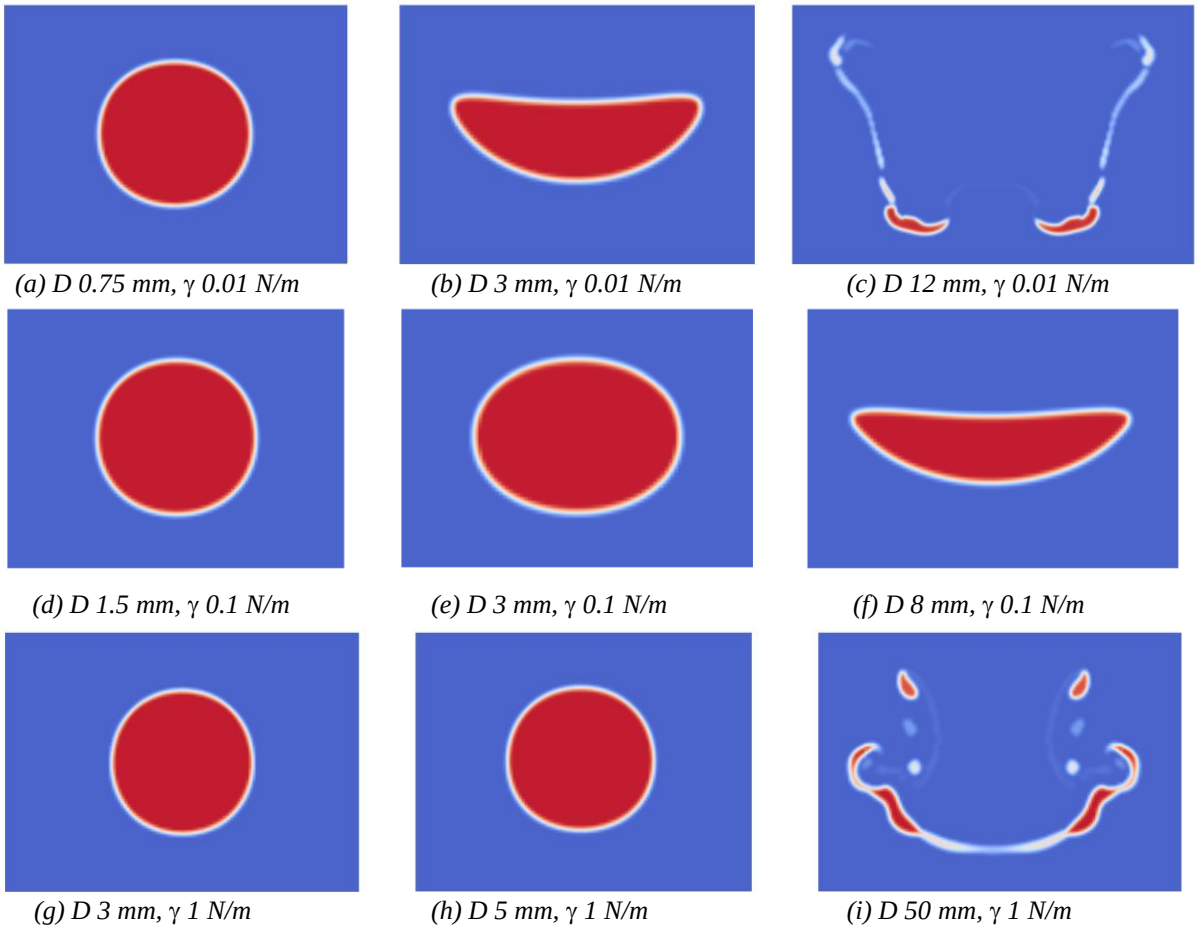

(a) D 0.75 mm, γ 0.01 N/m *(b) D 3 mm, γ 0.01 N/m* *(c) D 12 mm, γ 0.01 N/m*

(d) D 1.5 mm, γ 0.1 N/m *(e) D 3 mm, γ 0.1 N/m* *(f) D 8 mm, γ 0.1 N/m*

(g) D 3 mm, γ 1 N/m *(h) D 5 mm, γ 1 N/m* *(i) D 50 mm, γ 1 N/m*

Figure 10: Droplet shapes at end of computational model runs (captions correspond to Figure 8)

Results from computational modelling of droplet settling are seen to agree well with previously published qualitative and quantitative data on the subject, suggesting that the methodology in use is valid here.

3.4 Model results – intra-particle electromagnetic forces

In order to study the effect of electromagnetic forces in isolation, gravitational forces were then set to zero in the computational model leaving only MHD forces acting on the entrained droplet. This conveniently results in both the N_{Eo} and N_{Mo} parameters reducing to zero, with the droplet shape and behaviour therefore being completely characterized by a single dimensionless parameter, the electromagnetic Eötvös number N_{EM}. The current density field far from the droplet, j_0, acts vertically downward through the model region

Variables used for this set of cases are shown in Table 3.

Table 3: Variables used for MHD-only cases

Parameter	*Value*	*Parameter*	*Value*
D	0.1 – 20 mm	γ	0.1 - 1 N/m
μ_S	0.1 Pa.s	ρ_s	3500 kg/m^3
μ_M	0.006 Pa.s	ρ_m	7000 kg/m^3
j_0	2 x 10^5 - 1 x 10^6 A/m^2	μ_0	4π 10^{-7} N/A^2
κ_s	66.67 (Ωm)$^{-1}$	κ_m	5 x 10^7 (Ωm)$^{-1}$
Mesh resolution	25000 - 50000 elements	Mesh dimensions	(2.5D - 5D) x 5D

3.4.1 Metal droplets in slag

For the case of a metal droplet entrained in a slag matrix phase, the electromagnetic forces resulting from the concentration of current density in the droplet causes a “pinch” effect – the droplet is squeezed from around the circumference perpendicular to the current density vector in the bulk slag. This can result in either deformation of the droplet into an oblate ellipsoid, or breakup and disintegration of the droplet into smaller fragments. An example of the

latter case is shown in Figure 11.

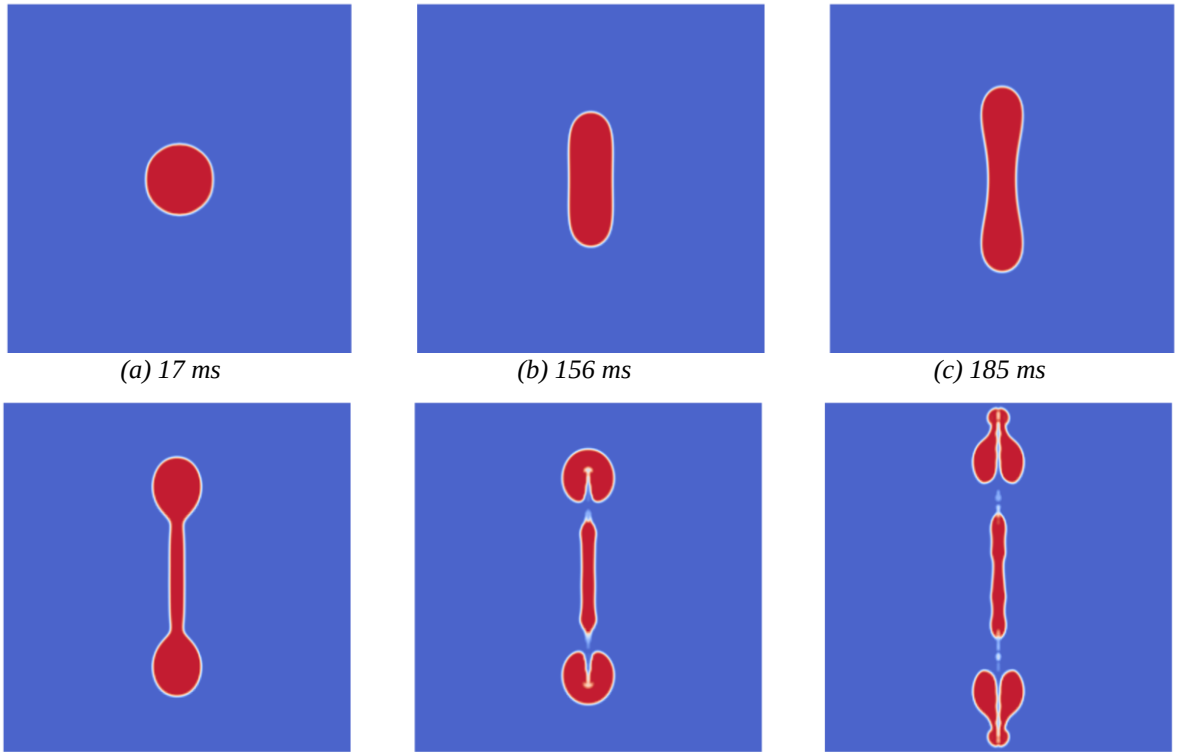

(a) 17 ms *(b) 156 ms* *(c) 185 ms*

(d) 200 ms *(e) 203 ms* *(f) 206 ms*

Figure 11: Evolution of metal droplet shape over time, D = 6 mm, $j_0 = 10^6$ A/m^2, γ = 0.1 N/m

The electromagnetic deformation of the droplet proceeds slowly at first, but accelerates rapidly as the droplet surface becomes concave and then separates into fragments. Overall the process is quite rapid, with the droplet disintegrating after only 200 ms in this case.

The final steady-state shape of the droplet (if it exists) was estimated by measuring the ratio of the droplet's horizontal axis to its vertical axis either at the end of the simulation (500 ms) or at the point of disintegration. N_{EM} was varied by changing the droplet diameter between 0.1 mm and 10 mm while keeping all other parameters constant ($j_0 = 10^6$ A/m^2, γ = 0.1 N/m). The result of this calculation for all model cases tested is shown in Figure 12.

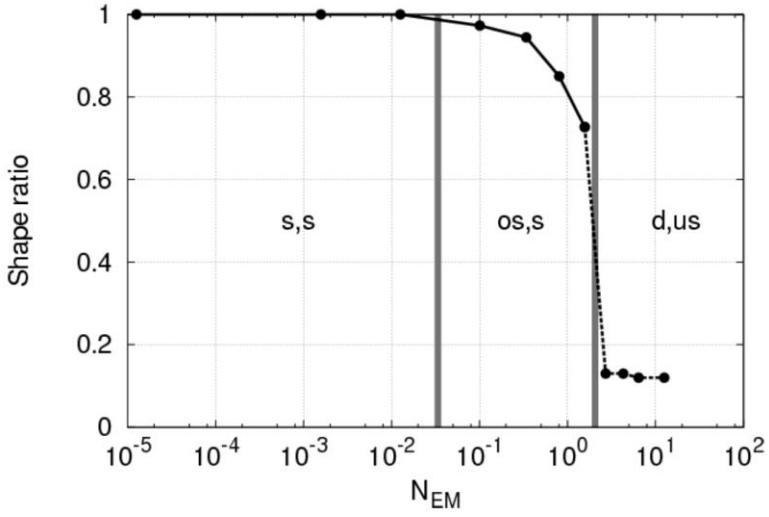

Figure 12: Variation of droplet shape ratio with N_{EM} (s,s: spherical and steady-state, os,s: prolate spheroid, steady-state, d,us: disintegration, unsteady-state)

It was observed that for N_{EM} below approximately 0.03, electromagnetic forces are very small and the droplet retains its spherical shape. For N_{EM} between 0.1 and 2, the surface tension and electromagnetic forces are of similar magnitudes, and the droplet is distorted into an oval shape. For N_{EM} above 2, the electromagnetic forces dominate the

fluid flow in the vicinity of the droplet and act to pinch and disintegrate it, with highly dynamic flow patterns resulting.

Examples of droplet shapes from computational model simulations in each zone in Figure 12 are shown in Figure 13.

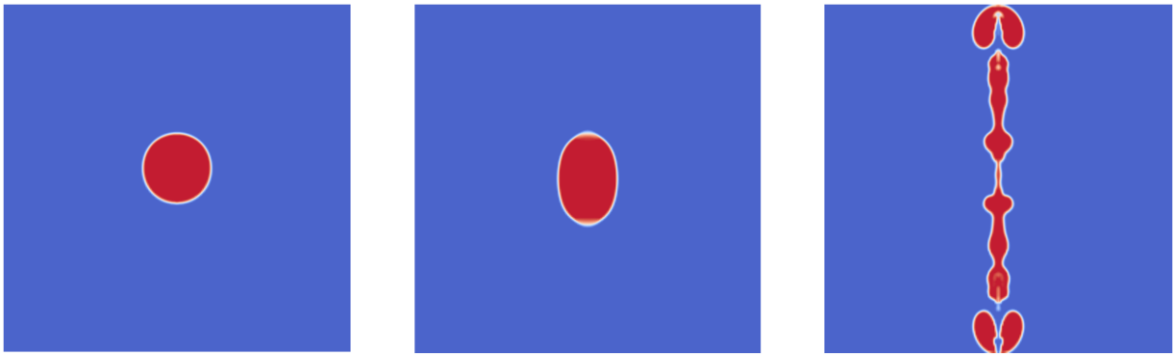

(a) D = 1 mm (N_{EM} = 0.0126) *(b) D = 5 mm (N_{EM} = 1.57)* *(c) D = 10 mm (N_{EM} = 12.6)*

Figure 13: Droplet shapes at end of simulation ($j_0 = 10^6$ A/m^2, γ = 0.1 N/m)

It can be seen that the distortion of the droplet increases rapidly with increasing N_{EM}, until a critical point at which the system becomes unsteady and the droplet disintegrates into smaller particles.

3.4.2 Slag droplets in metal

Just as metal droplets may become entrained into the slag phase by mechanical stirring and other mechanisms, it is possible for slag droplets to become entrained in the metal phase. In this case, the droplet forms a highly resistive inclusion and the current density field in the metal is diverted around it. It is interesting to note that due to this, the electromagnetic forces act in an opposite manner to those in the case of an entrained metal droplet – they "squash" the droplet, pulling it out radially along the circumference perpendicular to the current density vector in the bulk metal.

Computational models for the entrained slag droplet problem were set up and run using the parameters in Table 3. Droplet shapes at the end of the simulations are shown in Figure 14.

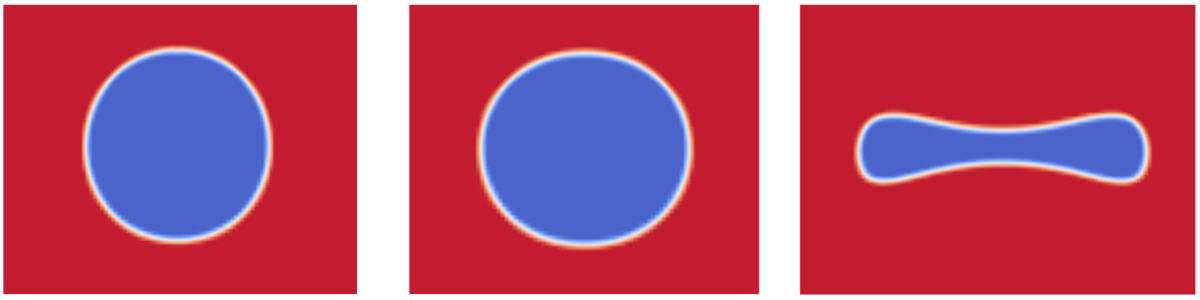

(a) D = 5 mm *(b) D = 10 mm* *(c) D = 20 mm*

Figure 14: Droplet shapes at end of simulation, $j_0 = 10^6$ A/m^2, γ = 0.1 N/m

As increasing the droplet diameter increases N_{EM}, the shape becomes first a flattened sphere, and eventually a toroid. At a diameter of 20 mm, the droplet is unsteady and continues to expand into a ring-shaped structure.

It is interesting to observe that the droplet shape is only affected at larger diameters (higher N_{EM}) than in the case of metal droplets entrained in slag. This is in accordance with the fact that the distortion of the current density field is only one half as large as it is in the metal droplet case, as noted in Section 2.2.

3.5 Model results – electromagnetic forces combined with gravity

For the full droplet MHD model, both the intra-particle electromagnetic forces as well as gravity must be considered. Model conditions are as per Table 3, with the addition of gravitational acceleration of 9.81 m/s^2 in the vertical direction. Due to the large possible parameter space presented by N_{EM}, N_{Mo} and N_{Eo}, simulations were conducted for a range of N_{EM} and N_{Eo} only by varying the diameter of the droplet while keeping all other variables fixed in order to gain a basic understanding of the interaction between the various forces.

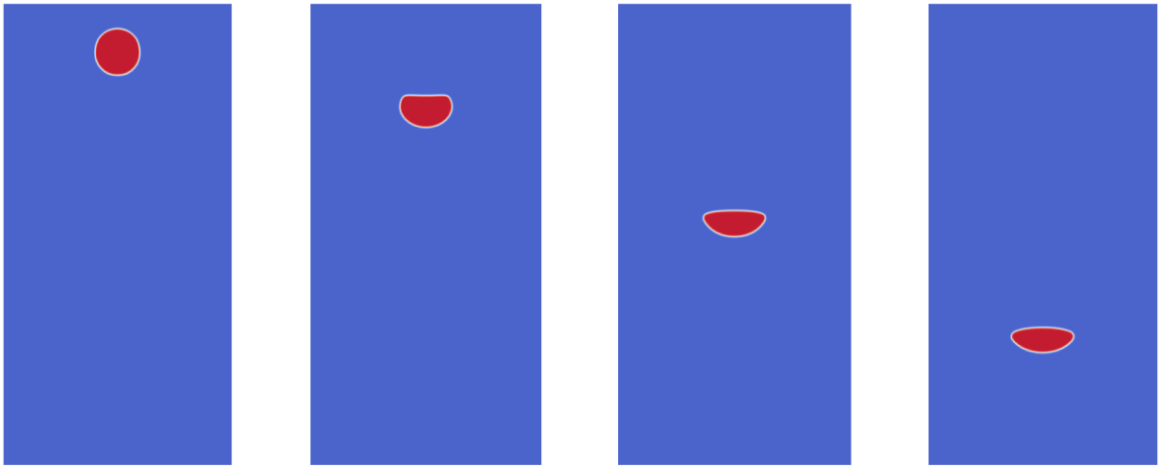

(a) 17 ms *(b) 99 ms* *(c) 201 ms* *(d) 302 ms*

Figure 15: Development of phase field, D = 6 mm, $j_0 = 10^6$ A/m^2, γ = 0.1 N/m (N_{Eo} = 12.3, N_{Mo} = 7.01 x 10^{-5}, N_{EM} = 2.71)

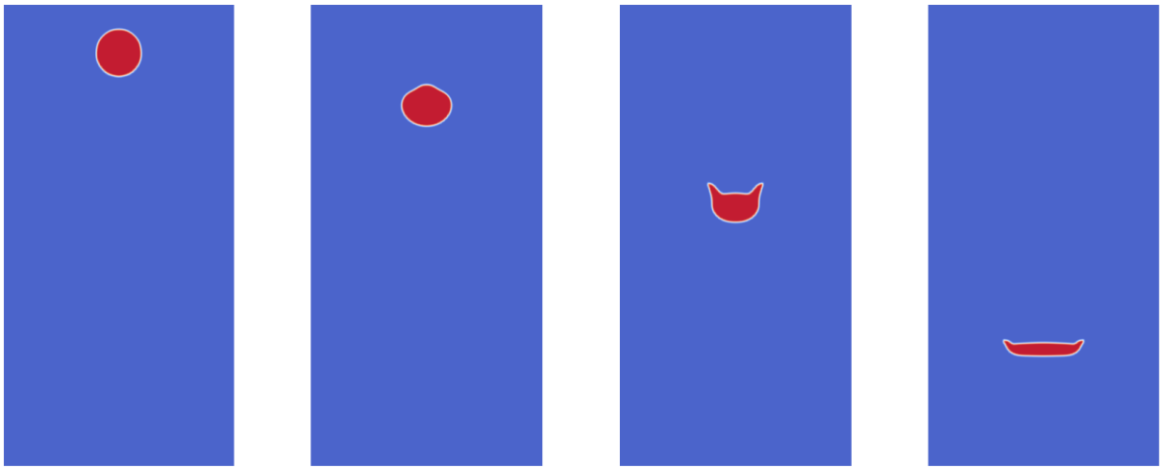

(a) 17 ms *(b) 100 ms* *(c) 181 ms* *(d) 298 ms*

Figure 16: Development of phase field, D = 8 mm, $j_0 = 10^6$ A/m^2, γ = 0.1 N/m (N_{Eo} = 22.0, N_{Mo} = 7.01 x 10^{-5}, N_{EM} = 6.43)

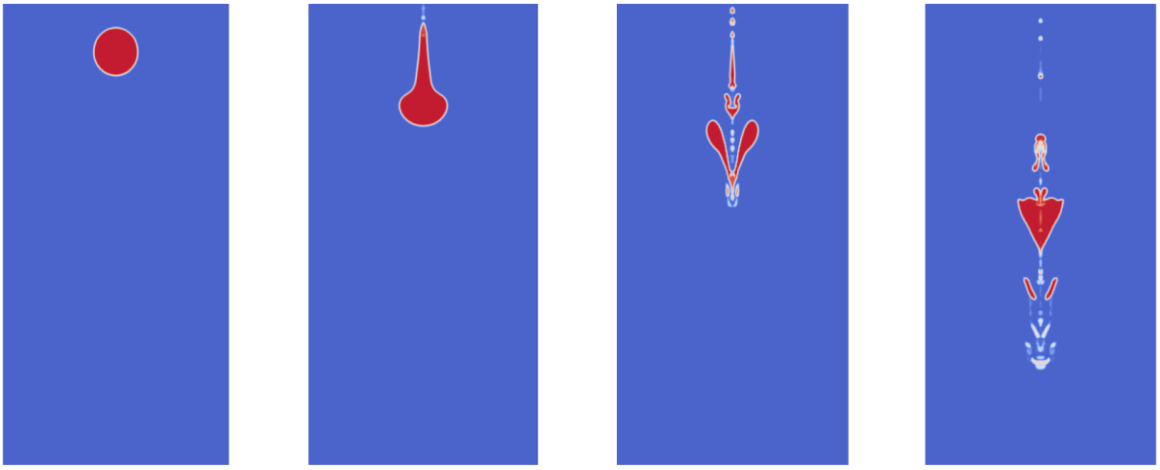

(a) 18 ms *(b) 101 ms* *(c) 125 ms* *(d) 200 ms*

Figure 17: Development of phase field, D = 10 mm, $j_0 = 10^6$ A/m^2, γ = 0.1 N/m (N_{Eo} = 34.3, N_{Mo} = 7.01 x 10^{-5}, N_{EM} = 12.6)

Results showing the evolution of the phase field for three different cases are shown in Figure 15, Figure 16, and

Figure 17. It is interesting to note that the addition of settling due to gravity to the MHD droplet model stabilizes the shape deformation due to electromagnetic forces to some degree; this is most likely due to the fact that gravitational settling generally acts to flatten the droplet along the gravitational acceleration vector, whereas the electromagnetic forces act to compress the droplet along the current density vector. In these simulations, both vectors are aligned and therefore the forces act counter to each other. This is borne out in the model results by the droplet remaining intact up to approximately N_{EM} = 6.5 when gravitational settling is present, but disintegrating completely under the action of electromagnetic forces by N_{EM} ~ 2 when it is not.

The strength of this effect will depend not only on the three dimensionless parameters used here, but also on the angle between the gravity vector and the local current density vector – in operating electric furnaces, particularly AC furnaces where current paths travel between electrodes instead of downward through the vessel, the angle may be up to 90° and the droplet stabilization effect may be reduced or even reversed in regions where this is the case. Differences are frequently observed in the rates of settling and phase separation between AC and DC furnace designs, though whether this is primarily due to electromagnetic effects or other phenomena (for example, electro-capillary droplet motion) is less easy to determine.

3.6 Model results – attraction between two droplets

For the study of the interactions between multiple entrained droplets, three-dimensional modelling is necessary. Such models are extremely computationally demanding, and require high-performance computing resources in order to run effectively. Dynamic adaptive meshing based on the phase fraction field was also used to increase performance. Due to the very long runtimes of the 3D models, only a limited number of results have been generated at this stage.

Table 4 shows the conditions used for the droplet interaction model cases. The droplets are separated by the centre-to-centre distance x_s, along the x-axis. Gravity and other external forces are not considered in these models, and electric current flows downward in the z direction.

Table 4: Variables used for droplet attraction models

Parameter	*Value*	*Parameter*	*Value*
D	6 mm	γ	0.1 N/m
μ_S	0.1 Pa.s	ρ_s	3500 kg/m^3
μ_M	0.006 Pa.s	ρ_m	7000 kg/m^3
j_0	1 x 10^6 A/m^2	μ_0	4π x 10^{-7} N/A^2
κ_s	66.67 (Ωm)$^{-1}$	κ_m	5 x 10^7 (Ωm)$^{-1}$
Mesh resolution	Up to 1000000 elements	Mesh dimensions	(2.5D + x_s) x 2.5D x 10D
x_s	12 mm, 18 mm, 24 mm		

Figure 18 and Figure 19 show a plane section through the phase field along the x-axis at various times, for the two cases of 12 and 24 mm separation between droplets. A contour at a metal fraction of 0.5 gives an indication of the three-dimensional shape of the droplets.

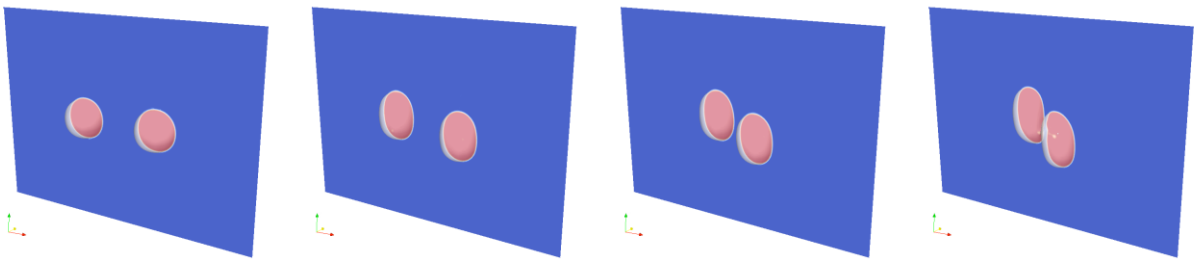

(a) 0 ms *(b) 202 ms* *(c) 411 ms* *(d) 486 ms*

Figure 18: Evolution of droplet shapes and positions, x_s = 12 mm

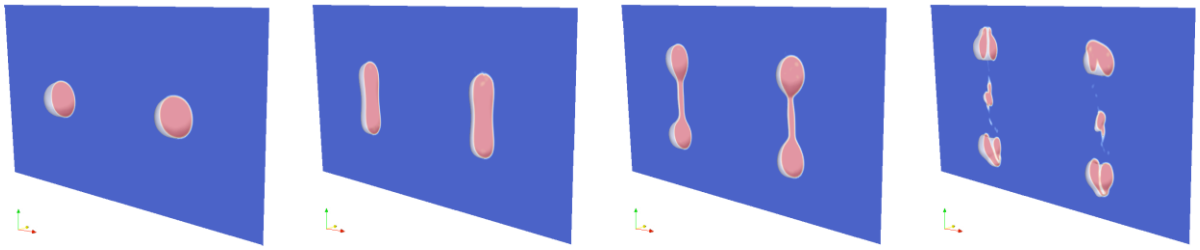

(a) 0 ms *(b) 405 ms* *(c) 440 ms* *(d) 451 ms*

Figure 19: Evolution of droplet shapes and positions, x_s = 24 mm

There are appreciable differences in the droplet behaviour at different separations. At very small separations of the order of the droplet diameter the inter-particle electromagnetic attraction is strong enough to draw the droplets together, whereas at only slightly larger separations the attraction falls away rapidly. This can be seen in Figure 20, which plots the droplet separation over time.

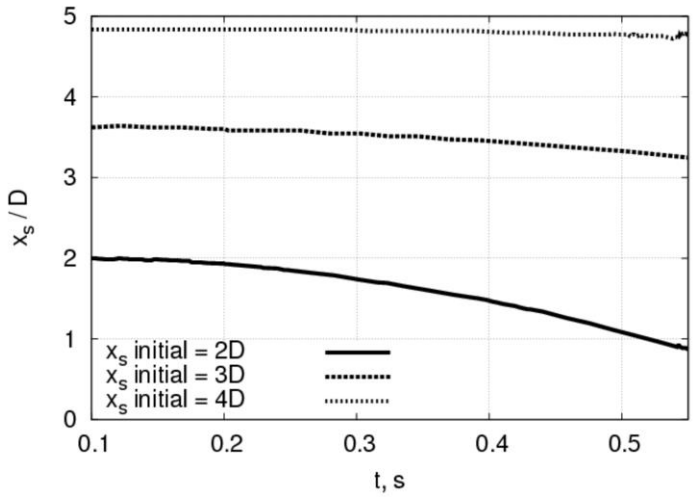

Figure 20: Droplet separation over time for different initial separations

Two additional effects are seen in the model results. The first is that even though the droplets move toward each other and make physical contact in the case of very narrow initial separations, the closing velocities are very low. Combined with the relatively high interfacial surface tensions typical of metal-slag systems, this means that the droplets do not actually coalesce but rather bounce off each other in an elastic or semi-elastic collision (cf. Figure 18d).

The second effect is that the additional inter-particle forces appear to partially balance the intra-particle forces at narrow separation distances. For a diameter of 6 mm the droplet is expected to disintegrate under the action of the intra-particle electromagnetic forces, as is the case in Figure 11 and Figure 19 however, droplets of the same size are seen to remain intact up to the point of collision in Figure 18. As in the case of gravity-stabilized MHD droplets, this stabilization effect is strongly related not only to the droplet properties but also to the separation distance between droplets and also the angle between the background current density vector and the line between droplet centres.

4 CONCLUSIONS

An aspect of the phase separation problem in electric arc furnaces, the flow dynamics of entrained droplets, has been successfully studied using a combination of mathematical analysis and computational modelling. Several insights were gained into the relative strength of the various forces acting on droplets of one phase entrained in another. At very small droplet diameters typical of prills and micro-inclusions surface tension forces generally dominate, while at larger diameters typical of phase mixing in regions of high stirring energy (such as near to plasma arcs) electromagnetic forces can become significant.

The dynamic behaviour and shape of single droplets settling under gravity was successfully used to test and validate the computational model across a range of the dimensionless parameters N_{Eo} and N_{Mo}. It was seen that when electromagnetic forces act in isolation, the droplet shape may be characterized by a single dimensionless parameter, N_{EM}. At high values of N_{EM} droplets disintegrate into smaller fragments under the action of the electromagnetic forces, while at low values they remain intact and form oval or spherical shapes. A stabilizing effect was observed when the combination of gravitational and electromagnetic forces was modelled. This effect was visible at higher values of N_{EM} and

N_{Eo}, such that large droplets settling in regions through which high current densities are passing may remain intact for longer periods of time.

Inter-particle attraction between metal droplets entrained in a slag phase is possible, and was quantified using a simplified mathematical model. The effect was seen to be strongly dependent on the separation distance between particles as well as the particles' diameter, but is generally much smaller than the intra-particle electromagnetic forces. Three-dimensional computational modelling of this problem showed the effect of particle separation, and also identified a secondary electromagnetic shape stabilization effect occurring when droplets are in close proximity to one another.

This work is exploratory in nature, and further study is needed. In particular, additional modelling work is required in order to more completely quantify the effect of the full $N_{Eo} - N_{Mo} - N_{EM}$ parameter space for the behaviour of single droplets. The three-dimensional behaviour of multiple droplet systems also presents several phenomena of interest and would benefit from further examination. Together with additional computational modelling work, it is highly recommended that experimental work using cold models be used to provide additional validation of the computational modelling tools.

5 ACKNOWLEDGEMENTS

This paper is published by permission of Mintek. The author also gratefully acknowledges access to HPC facilities at the CSIR Centre for High Performance Computing during the development and testing of the computational models.

6 REFERENCES

[1] Jones, R.T. and Curr, T.R., "Pyrometallurgy at Mintek", Proceedings of the SAIMM Southern African Pyrometallurgy 2006 Conference, Johannesburg (South Africa), 5-8 March 2006, pp. 127-150.

[2] Bowman, B., "Properties of arcs in DC furnaces", Proceedings of the 52nd Electric Furnace Conference, Nashville (USA), 13-16 November 1993, pp. 111-120.

[3] Reynolds, Q.G., "Application of multiphase computational fluid dynamics to the plasma arc impingement problem in DC furnaces", Proceedings of the 9th South African Conference on Computational and Applied Mechanics, Somerset West (South Africa), 14-16 January 2014, article #26.

[4] Warczok, A., Utigard, T., "The effects of alternating and direct currents on the rate of slag cleaning", CIM Annual Meeting: Proceedings of Non-ferrous Pyrometallurgy - Trace metals, furnace practices and energy efficiency, Edmonton (Canada), 23-27 August 1992, pp. 403-419.

[5] Warczok, A., Riveros, G., "Effect of electric and magnetic fields on metallic inclusions in a liquid slag", Proceedings of the TMS Annual Meeting, San Diego (USA), 2-6 March 2003, pp. 224-229.

[6] Dal, I., Li, N., and Grimsey, E.J., "The reduction of nickel slag by graphite electrodes with AC and DC currents", Proceedings of the Nickel-Cobalt International Symposium, Sudbury (Canada), 17-20 August 1997, pp. 77-92.

[7] Warczok, A. and Riveros, G., "Slag cleaning in crossed electric and magnetic fields", Minerals Engineering, 20 (2007), pp. 34-43.

[8] Hyers R.W., Trapaga, G., and Abedian, B., "Laminar-Turbulent Transition in an Electromagnetically Levitated Droplet", Metallurgical and Materials Transactions B, 34B (2003), pp. 29-36.

[9] Amaya-Bower, L. and Lee, T., "Single bubble rising dynamics for moderate Reynolds number using Lattice Boltzmann Method", Computers & Fluids, 39 (2010), pp. 1191-1207.

[10] Clift, R., Grace, J.R., and Weber, M.E., "Bubbles, Drops, and Particles", Academic Press Inc., New York (USA), 1978.

[11] OpenFOAM, http://www.openfoam.org, accessed November 2014.

[12] Bhaga, D. and Weber, M.E., "Bubbles in viscous liquids: shapes, wakes, and velocities", Journal of Fluid Mechanics, 105 (1981), pp. 61-85.